

Full In-plane Strain Tensor Analysis using the Microscale Ring-core FIB milling and DIC Approach

Alexander J. G. Lunt^{a*} (alexander.lunt@chch.ox.ac.uk), Enrico Salvati^a (enrico.salvati@eng.ox.ac.uk), Lifeng Ma^b (malf@mail.xjtu.edu.cn), Igor P. Dolbnya^c (igor.dolbnya@diamond.ac.uk), Tee K. Neo^d (neophyte@singnet.com.sg) & Alexander M. Korsunsky^a (alexander.korsunsky@eng.ox.ac.uk)

- ^{a.} Department of Engineering Science, University of Oxford, Parks Road, Oxford, Oxfordshire, OX1 3PJ, United Kingdom.
- ^{b.} S&V Lab, Department of Engineering Mechanics, Xi'an Jiaotong University, 710049, China.
- ^{c.} Diamond Light Source, Harwell Science & Innovation Campus, Didcot, Oxfordshire, OX11 0DE, United Kingdom.
- ^{d.} Specialist Dental Group, Mount Elizabeth Orchard, 3 Mount Elizabeth, #08-03/08-08/08 10, Singapore 228510.

* Corresponding author

Abstract

Full In-plane Strain Tensor (FIST) analysis at the micro-scale is crucial for improving the evaluation of residual stress and the understanding of the origins of mechanical failure in many applications ranging from civil structures to energy systems and micro-electronics. This study presents the analytical background and experimental implementation of a Focused Ion Beam (FIB) milling and Digital Image Correlation (DIC) based technique that uses material removal and strain relief monitoring to perform precise, reliable and rapid quantification of micro-scale residual stress. The nature of semi-destructive FIB milling overcomes the main limitations of X-Ray Diffraction (XRD) strain tensor quantification: unstrained lattice parameter estimates are not required, analysis is performed in within a precisely defined 3D microscale volume, both amorphous and crystalline materials can be studied and access to X-ray/neutron facilities is not required.

The FIST FIB milling and DIC experimental technique is based on extending the interpretation of strain relief observed for the ring-core milling geometry to quantify the strain variation with azimuthal angle. The approach benefits from the high magnitude of strain relief, excellent precision and the simplicity of the analytical approach associated with this method. In-plane strain analysis is reported for a sample of commercial interest: a porcelain veneered Yttria Partially Stabilised Zirconia (YPSZ) dental prosthesis, for which the results were also compared with micro-beam synchrotron X-ray diffraction. Since the two methods sample different gauge volumes and mechanical states (approaching plane stress for ring-core milling and through-thickness averaging that approaches plane strain for XRD), the important matter of correlating the two sets of measurements arises and requires addressing. Complex variable and Finite Element (FE) methods are used to connect the two states, demonstrating that valid comparisons can be drawn. The analysis revealed excellent agreement between the principal stress orientation and values, led to realistic residual stress estimates which closely matched literature measurements ($\sigma_{Av} \approx 460$ MPa) and produced upper and lower bounds for the (101) interplanar crystal lattice spacing of YPSZ in the range $2.9586 - 2.9596$ Å, closely matching published values.

Highlights

- Full in-plane strain tensor measured by ring-core Focused Ion Beam (FIB) milling
- Absolute strain measurement at the μm -scale for amorphous & crystalline materials
- Comparative X-ray diffraction study validates experimental FIB results
- Lattice parameter and stress state in Zr prosthesis sample match literature values
- Surface vs bulk residual stress state relationships was identified and validated

Keywords

Residual stress

Electron microscopy

Finite elements

Nondestructive evaluation

Ceramic material

1

¹ FIST – Full In-plane Strain Tensor
FIB – Focused Ion Beam
DIC – Digital Image Correlation
XRD – X-Ray Diffraction
YPSZ – Yttria Partially Stabilised Zirconia
FE – Finite Element
SEM – Scanning Electron Microscopy
MBLEM – Multi-Beam Laboratory for Engineering Microscopy
ROI – Region Of Interest

1. Introduction

The term residual stress refers to the presence of internal forces within an object in the absence of external load. The interaction between these forces and applied loading is responsible for the mechanical failure of a broad range of engineering components and systems [1]. Stresses of this type can be induced by a range of different mechanical phenomena, from inhomogeneous deformation in polycrystalline aggregates [2, 3], plastic zones induced at crack tips [4, 5] to thermal expansion mismatch [6] and solid state phase transformations [7, 8]. Alternatively, residual stresses can be intentionally introduced into a component in order to overcome the influence of external loading, typically through the addition of compressive stress using techniques such as peening [9, 10] or rolling [11]. Precise, reliable and quantitative measurement of residual stresses is therefore necessary in order to improve understanding of failure and facilitate improved component designs.

Stress is defined by the average force acting across a particular cross section within any given body, and therefore this mechanical parameter is intrinsically linked to the length scale over which it is defined. In the case of macroscopic stress measures, short-range fluctuations in force are averaged out over large areas, which severely limits the insight available into the local stress magnitudes. For this reason the recent developments in residual stress analysis have focused on attaining higher spatial resolution to quantify stress at precise locations where failure is most likely to occur [12, 13]. These advances have been used to develop improved designs and to understand failure in a wide range of components from carbon fibre composite systems [14], to silicon nanowires for microelectronic devices [15] and thin film solar cell applications [16].

In some studies, the determination of an average stress component is sufficient to provide the answers required. However, the improved insight offered by the full quantification of residual stress variation with orientation is often necessary [17, 18]. In recent years, strain tensor determination and stress calculation based on neutron [19] and X-Ray Diffraction (XRD) [20-23] measurements has become a well-established technique. Despite the many benefits of these approaches, there are a number of well-known limitations associated with these methods. Firstly, precise estimates of

unstrained lattice parameters are required; this is particularly difficult in the case of high resolution studies where local variations in elemental composition may also induce ‘chemical’ changes of this parameter over similar length scales. Secondly, these high precision techniques can only be applied to crystalline materials and therefore equivalent analysis cannot be performed in amorphous substrates. Another difficulty is associated with the limited 3D resolution that can be obtained. This is due to the large penetration depths of neutron and high energy X-ray beams typically required in these studies. Approaches involving tomographic [24] and grazing angle [25] methods have been developed to overcome this limitation at the expense of increased processing complexity, time and reduced precision. Finally, these methods typically require access to large scientific facilities which severely restricts the number of potential applications that can be studied.

In recent years, new techniques based on Focused Ion Beam (FIB) milling of a surface of interest and Digital Image Correlation (DIC) of the resulting Scanning Electron Microscopy (SEM) images have been developed to overcome the limitations associated with diffraction based methods [12, 26]. These approaches are capable of determining residual stress within precisely defined microscale gauge volumes and provide absolute estimates of stress in both crystalline and amorphous samples without the need for unstrained lattice parameter values. The increasing availability of FIB-SEM systems also ensures that these approaches can be readily implemented at thousands of laboratories across the world.

Different FIB milling and DIC geometries have been proposed typically based on microscale versions of well-established macroscopic semi-destructive residual stress evaluation techniques. These include surface slotting [27], dual slotting (also known as H-bar milling) [28], blind hole [29] and ring-core milling [30]. These different geometries were developed to meet the needs of a particular application. However, only the blind hole and ring-core drilling techniques have the isotropic geometry required to provide insight into the angular variation of in-plane stress at a single measurement location.

A critical comparison between the hole drilling and ring-core methodologies reveals that although the geometry of the ring-core approach makes the analysis marginally more computationally difficult, the residual stress estimate obtained using this technique is more precise, more sensitive to low magnitude residual stresses and has a much more precisely defined gauge volume [26, 31-33]. The ring-core geometry has also recently been extended to quantify Poisson's ratio at micrometre resolution [34] as well as the lateral [12] and depth [35] variation of residual stresses.

Estimates of the in-plane stress tensor have previously been performed using the ring-core approach by quantifying the strain relief in three orientations (typically denoted as 0° , 45° and 90° with respect to a chosen direction) and fitting these results to Mohr's circle formulation [12]. The main limitation preventing the calculation of other orientations (to improve the precision of the strain tensor estimate) has been the lack of automation in the DIC methods required to quantify strain in a given direction. However, recent advances in error evaluation and propagation, outlier removal and correlation analysis have for the first time enabled strain quantification to become a rapid, precise and fully automated process [26]. Using this automated approach, this study demonstrates the experimental and analytical steps necessary to evaluate the strain relief variation as a function of orientation angle, thereby enabling Full In-plane Strain Tensor (FIST) analysis. Provided that the elastic constants of the system under consideration are known fully, the corresponding residual stress variation can then be determined from this in-plane strain tensor.

XRD has previously been successfully used to validate the results of residual stress estimates produced by ring-core milling both in terms of the average [36] and stress components in two orthogonal directions [12]. In this study the results of FIST ring-core analysis will be compared with those obtained using high energy transmission XRD performed on a dental prosthesis sample. The stress states associated with these two experimental approaches are known to be different: in the case of surface ring-core milling the stress condition is close to plane stress, while XRD analysis provides an average of both the near surface (plane stress) and bulk (which is closer to conditions of

plane strain). Therefore in order to provide comparisons between these two techniques the analytical relationships between the two states determined using two different analytical methods and Finite Element (FE) simulations have been used to validate these relationships. This comparative approach also provides the upper and lower bounding limits of the lattice spacing of the underlying substrate material.

2. Material and methods

2.1. Sample selection and preparation

The sample selected for this experimental study was a Yttria Partially Stabilised Zirconia (YPSZ) dental prosthesis manufactured from Wieland Dental Zenotech[®] Zr Bridge [37] by dental technicians at the Specialist Dental Group, Singapore. In order to reduce the hardness of the outer surface of the prosthesis, and thereby match the properties of natural teeth, the YPSZ copings were veneered with Ivoclar Vivadent IPS e.max[®] Ceram [38]. Multiple layers of this aqueous porcelain slurry are applied and fired into a veneer in order to tailor the appearance of the prosthesis and produce an aesthetically pleasing finish.

Despite its advantages, this manufacturing process has recently been shown to induce residual stresses in the near-interface regions of both YPSZ and porcelain [39-42], leading to the primary failure mode of these prosthesis: near interface chipping of the porcelain veneer [43, 44]. The origins of this residual stress state are associated with the YPSZ tetragonal to monoclinic phase transformation [45-47], elemental diffusion across the interface [48] as well the impact of high temperature creep in the near-interface porcelain [49, 50].

This system was selected for the comparative XRD and FIB milling strain tensor quantification study as it embodies the key requirements to enable effective comparisons to be drawn:

- 1. A well characterised high magnitude residual stress state which is contained within a known micrometre-scaled region.** This ensures that the length-scale variation of residual stress is comparable to the gauge volumes of the two experimental techniques and is of sufficient magnitude that it can be reliably detected by both XRD and FIB milling methods.

Further, the proximity of this stress measurement location to the YPSZ-porcelain interface ensures that marker placement and X-ray beam alignment can be conducted precisely.

2. A nominally biaxial uniform residual stress distribution. The presence of the YPSZ-porcelain interface dominates the mechanical state of this region and ensures that variations in residual stress are primarily dependent on the distance from this boundary. This means that the different gauge volume sizes and averaging associated with the two experimental techniques can be performed in directions corresponding to appreciably uniform stress states. This ensures that the comparison between the two stress states is valid, as discussed in detail in Section 3.2.

3. A nanocrystalline substrate which diffracts effectively under X-ray illumination. In order to perform strain tensor quantification using X-ray powder diffraction, smooth low noise diffraction peaks (or Debye-Scherrer rings on an area detector, in other words) are required. The nano-crystalline nature of YPSZ and its strong X-ray scattering ensures that high quality diffraction patterns are collected. Further, the random texture (confirmed by XRD) and nano-scale grain sizes of YPSZ ensure the validity of the isotropic relaxation assumption used in the ring-core analysis.

The location selected for strain tensor analysis was a distance of $50\ \mu m$ from the porcelain interface within the YPSZ. This position is known to have moderate levels of residual stress but is sufficiently far from the interface that the YPSZ phase transformation and elemental diffusion effects are not present at this location [47, 48]. This ensures that lattice spacing variation (d^{hkl}) is not influenced by these two factors and is therefore representative of the bulk YPSZ atomic structure.

The other benefit of choosing a position at $50\ \mu m$ from the interface is that the magnitude of the eigenstrain source of residual stress at this location can be approximated as zero. The near-interface response of this system to heat treatment and stressing induces eigenstrain (permanent inelastic strain) through transformation, elemental diffusion and creep. However, this behaviour is confined to a very narrow boundary layer with a width in the order of $< 10\ \mu m$ from the interface

[45, 47]. This means that at $50\ \mu\text{m}$ from the interface only residual elastic strain is present. The validity of this approximation is important in the conversion between plane stress and plane strain behaviour as outlined in Section 3.2.

In order to facilitate access to the near-interface region, a cross section of the YPSZ prosthesis was obtained using a Buehler Isomet Diamond Saw (Figure 1). A slow rotational cutting speed of 25 rpm (on a 127 mm diameter blade) was selected to minimise the residual stresses induced during sample preparation. A metallurgical incremental grinding and polishing process concluded with colloidal silica finishing was then used to minimise the influence of sample preparation on the residual stress state. The final sample thickness was selected to be $115\ \mu\text{m}$ in order to maximise the intensity of the diffraction patterns collected during the synchrotron XRD experiment.

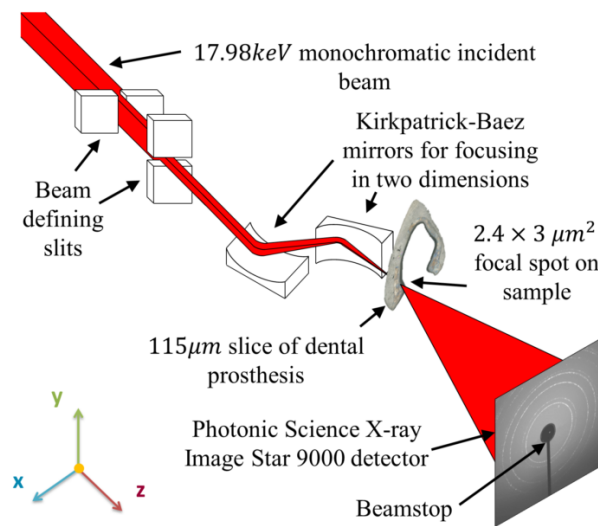


Figure 1. Schematic of synchrotron XRD experiment showing beam defining and focusing setup, sample oriented in a transmission geometry and a typical diffraction pattern.

2.2. Micro Focus XRD

Transmission powder XRD was performed at Beamline B16 (Diamond Light Source, UK) using the set up shown in the schematic in Figure 1. A $17.98\ \text{keV}$ monochromatic incident beam (just below the K-edge of zirconium) was selected in order to minimise absorption by the sample and a micro-focusing Kirkpatrick-Baez mirror pair arrangement was used to reduce the beam spot on the sample to $2.4 \times 3\ \mu\text{m}^2$. A Photonic Science X-ray Image Star 9000 detector placed in the

transmitted beam was used to collect complete 360° Debye-Scherrer diffraction patterns at a position 170 mm downstream from the sample.

A combination of optical alignment, X-ray imaging and identification of the interface through the differences in the scattering patterns of YPSZ and porcelain were used to determine the incident location of the beam on the sample to nanoscale precision. Diffraction patterns were then collected at a position $50\text{ }\mu\text{m}$ from the interface in the form of a 3×3 array covering an area of $7.2 \times 9\text{ }\mu\text{m}^2$ as shown in Figure 2. At each position a five minute exposure time was used to capture a high quality diffraction pattern.

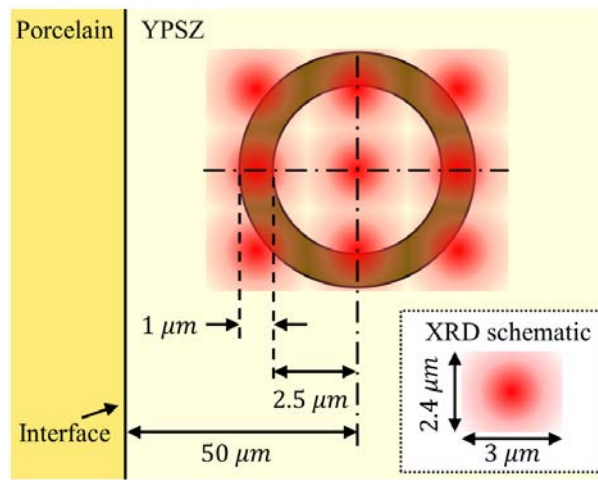


Figure 2. Schematic of residual stress analysis locations. The 3×3 array of XRD mapping points is shown superimposed over the $5\text{ }\mu\text{m}$ diameter ring-core milling geometry (with a $1\text{ }\mu\text{m}$ trench width). Both the XRD array and the ring-core geometry were centrally aligned at a distance of $50\text{ }\mu\text{m}$ from the YPSZ-porcelain interface.

Each diffraction pattern was then radially binned as a function of the azimuthal angle φ (as illustrated in Figure 3) to give line plots of scattered beam intensity against Q position averaged over 10° regions between 0° and 360° . For example, the 0° distribution was obtained from integrating between -5° and 5° . Beamstop shadowing was found to influence the profile obtained at the azimuthal angle of 270° and therefore the line profile obtained at 90° was used for this orientation.

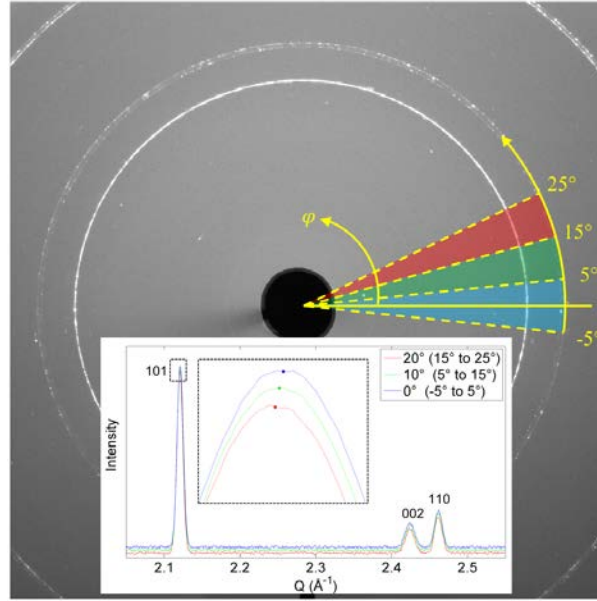


Figure 3. Radial integration of 2D diffraction pattern performed around azimuthal angle φ in 10° increments to produce 1D intensity distributions (insert). Gaussian peak fitting was performed on the tetragonal 101 diffraction peak in order to determine the peak centre position (indicated by markers) as a function of φ .

Gaussian peak fitting was then performed on the (101) peak of tetragonal zirconia. The high intensity of this peak ensured that the peak centres could be determined at the precision necessary to perform reliable strain tensor quantification. For example, the peak centres for the 0° , 10° and 20° positions have been highlighted by markers in Figure 3. Bragg's law was then used to convert the peak centre estimates to the lattice spacing in the (101) direction (d^{101}). This analysis was performed on all 9 diffraction patterns and the fitting confidence of each peak was used to determine a weighted average and the associated confidence interval for d^{101} at each angle φ .

2.3. FIB Milling and DIC

Ring-core FIB milling was performed on the sample using the Tescan Lyra 3 FIB-SEM at the Multi-Beam Laboratory for Engineering Microscopy (MBLEM, Oxford, UK) [51]. The prosthesis cross section was mounted on an SEM stub using silver paint and was sputter coated with 5 nm of gold-palladium in order to reduce sample charging. Applying a single fast pass of the focused ion beam across the surface of the sample causes the formation of a surface pattern that generates high

imaging contrast, as shown in Figure 4a. These patterns have previously been shown to facilitate effective DIC marker tracking during ring-core milling, without inducing stress state modification in the sample [26].

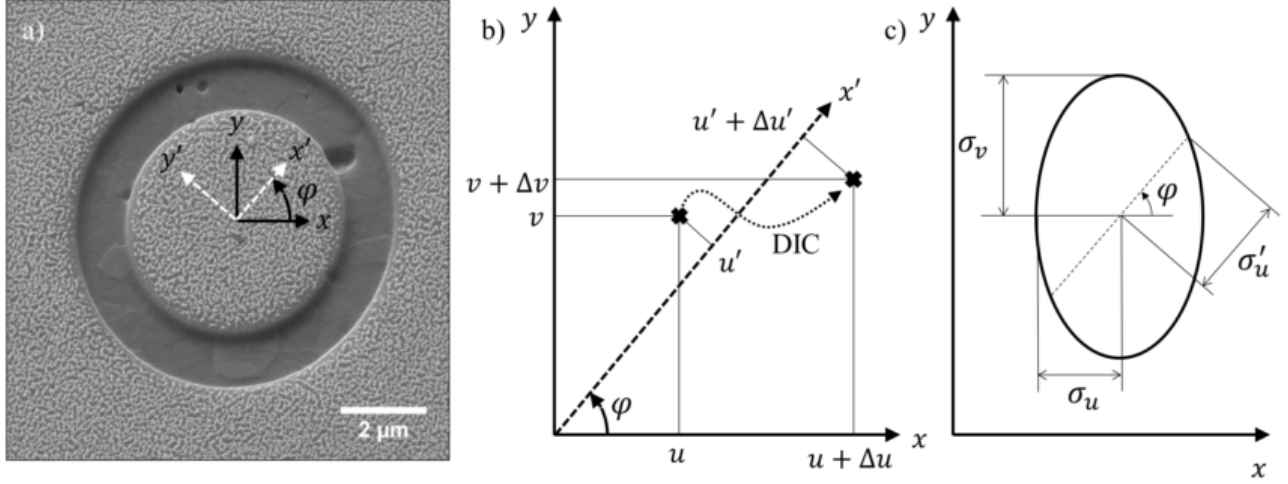


Figure 4. a) Secondary electron SEM image of the ring-core milling showing original (x, y) and rotated (x', y') coordinate systems for a given angle ϕ . b) Schematic showing a DIC marker shift of $(\Delta u, \Delta v)$ from starting position (u, v) and the corresponding position (u') and shift $(\Delta u')$ in the (x', y') coordinate frame. c) Schematic ellipse of DIC shift uncertainty showing the relationship between the standard deviations in the original (σ_u, σ_v) and the rotated coordinate system (σ'_u) .

A $5 \mu\text{m}$ diameter core was fabricated in the YPSZ by milling a $1 \mu\text{m}$ wide circular trench at a distance of $50 \mu\text{m}$ from the YPSZ-porcelain interface as shown in Figure 4a. A nominal milling depth of 125 nm was selected for each increment of the FIB milling process, and a 2048×2048 pixel secondary electron SEM image of the surface was captured at each step. In total 48 images were captured as a record of the core relaxation during FIB milling to a nominal depth of $6 \mu\text{m}$ in a time of ~ 30 minutes.

A modified version of the DIC code produced by Eberl et al. [52] was used to determine the strain relief at the surface of the core (micro-pillar) as a function of milling depth. Small amounts of drift were observed between each of the recorded images (with a maximum of $\sim 30 \text{ nm}$ between subsequent images) and low resolution DIC (drift correction) was performed on the exterior surface regions to correct for this effect. Subset DIC was performed on the island by placing several

hundred markers over the core centre where uniform strain relief is expected [53, 54]. Marker tracking was then performed using the approach outlined by Lunt et al. [26] in order to obtain the marker shift ($\Delta u, \Delta v$) relative to the start positions (u, v) in the (x, y) coordinate frame, along with the standard deviations of these shifts (σ_u and σ_v).

In-plane strain tensor quantification relies upon the precise determination of the strain magnitude variation as a function of angle φ . In the case of the ring-core milling approach this requires the determination of the core strain relief as a function of φ , and therefore the quantification of the DIC marker shift along an axis x' as shown in Figures 4a and 4b. For a given angle φ and marker starting position (u, v) the expression for the starting position along the x' direction is given as:

$$u' = u \cos \varphi + v \sin \varphi. \quad \text{Eq. 1}$$

Following automated marker tracking in the (x, y) coordinate frame, the shifts along the x' direction can be determined as:

$$\Delta u' = \Delta u \cos \varphi + \Delta v \sin \varphi. \quad \text{Eq. 2}$$

Quantification of the peak shift standard deviation in the direction parallel to the x' axis (σ'_u) is also necessary in order to determine strain uncertainty in a given direction. The elliptical representation of the uncertainty field proposed by Lunt et al. [26] in which the principal axes are aligned with the x and y directions (Figure 4c) can be used to estimate this value as:

$$\sigma'_u = \sqrt{\frac{\sigma_u^2 \sigma_v^2}{\sigma_v^2 \cos^2 \varphi + \sigma_u^2 \sin^2 \varphi}}. \quad \text{Eq. 3}$$

The rotated standard deviation estimates and marker shifts were then used as inputs into the strain relief quantification routine outlined by Lunt et al. [26]. In this approach, linear fitting of the relationship between u' and $\Delta u'$ is used to obtain the strain relief estimates associated with each milling depth ($\Delta \varepsilon$), as well as the corresponding standard deviations ($\sigma_{\Delta \varepsilon}$). Outlier removal is

necessary at this stage in order to remove poorly tracked markers and an automated multi-stage marker filtering routine was implemented:

1. The correlation coefficient was used to ensure that marker shift determination was only permitted in cases of high levels of similarity (correlation coefficients greater than 0.5) were observed between the DIC subset and the underlying image.
2. Thresholding based on the standard deviation of each marker position (σ'_u) was then performed to remove markers with low levels of confidence. It was found that removing markers with a standard deviation greater than 1.5 times the average value was effective for this data set.
3. Finally, the removal of markers moving relative to the expected displacement field was performed. This involved least squares fitting of the linear strain distribution expected across the island core and the calculation of the relative offset of all markers. Thresholding based on 1.5 times the average value of this relative offset was also found to be effective.

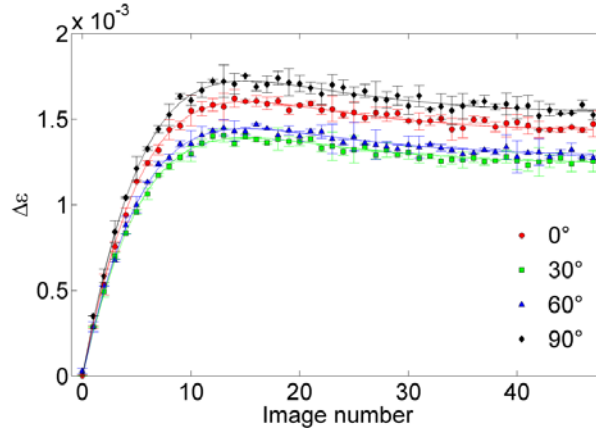


Figure 5. Strain relief against image number for data oriented at differing angles of φ . The original data and the 95% confidence error bars have been plotted along with the ‘master curve’ fitting given in Equation 4.

The relationship for the strain relief ($\Delta\varepsilon$) against milling depth was then fitted using the ring-core strain relief ‘master function’ originally published by Korsunsky et al. [30] (Figure 5):

$$f(\Delta\varepsilon_\infty, z) = 1.12\Delta\varepsilon_\infty \times \frac{z}{1+z} \left[1 + \frac{2}{(1+z^2)} \right], \quad \text{Eq. 4}$$

where $z = h/0.42d$, h is the milled depth, d is the core diameter and $\Delta\varepsilon_\infty$ is the full strain relief at an infinite milling depth. This representation of the relief was determined using FE simulations of the milling process in isotropic, homogenous materials and provides a quantitative estimate of magnitude and standard deviation ($\sigma_{\Delta\varepsilon_\infty}$) of the plateau observed in the strain relief curves $\Delta\varepsilon_\infty$ (Figure 5). This is the ultimate strain relief value for the material within the core once lateral constraint has been removed, and the material has returned to unstrained state. Its negative provides the estimate of the gauge-volume average residual strain in a given direction. For example, a positive core relief strain indicates that the original residual strain in the core was compressive.

The above analysis was implemented for φ values ranging from 0° to 360° in 10° steps in order to determine $\Delta\varepsilon_\infty$ and $\sigma_{\Delta\varepsilon_\infty}$ as a function of angle. As expected, it was found that the strain relief values and standard deviations obtained in opposite directions were equal, i.e. $\Delta\varepsilon_\infty^{0^\circ} = \Delta\varepsilon_\infty^{180^\circ}$ and $\sigma_{\Delta\varepsilon_\infty^{0^\circ}} = \sigma_{\Delta\varepsilon_\infty^{180^\circ}}$. This distribution of absolute strain was next used to determine estimates for the residual strain principal orientations and principal values as outlined in Section 3.2.

3. Theory/calculation

3.1. XRD strain determination

The tetragonal (101) lattice spacing estimates (d^{101}) obtained through XRD were used to quantify the lattice strain variation (ε^{101}) as a function of φ using the expression:

$$\varepsilon^{101}(\varphi) = \frac{d^{101}(\varphi) - d_0^{101}}{d_0^{101}}, \quad \text{Eq. 5}$$

where d_0^{101} is the unstrained lattice spacing for the 101 plane. Initially an estimate for this value ($d_0^{101} = 2.9582 \text{ \AA}$) was obtained from the short ($a = 3.605 \text{ \AA}$) and long ($c = 5.177 \text{ \AA}$) lattice constants of YPSZ provided in the literature [55], using the expression:

$$\left(\frac{1}{d_0^{hkl}} \right)^2 = \frac{h^2 + k^2}{a^2} + \frac{l^2}{c^2}, \quad \text{Eq. 6}$$

where $hkl = 101$.

A value for the standard deviation of the (101) unstrained lattice spacing ($\sigma_{d_0^{101}} = 0.0015 \text{ \AA}$) was also calculated based on the standard deviations of the short ($\sigma_a = 0.0010 \text{ \AA}$) and long ($\sigma_c = 0.0020 \text{ \AA}$) lattice constants provided in the literature:

$$\sigma_{d_0^{101}} = \frac{d_0^{101}}{2(c+a)} \sqrt{a^2 \sigma_c^2 + c^2 \sigma_a^2}. \quad \text{Eq. 7}$$

The standard deviation of the peak centre values ($\sigma_{d^{101}}(\varphi)$) were then used in combination with the standard deviation of the unstrained lattice spacing in order to obtain estimates of the standard deviation of the lattice strain ($\sigma_{\varepsilon^{101}}(\varphi)$):

$$\sigma_{\varepsilon^{101}}(\varphi) = \left(\frac{1}{d_0^{101}} \right)^2 \sqrt{(\sigma_{d^{101}}(\varphi) d_0^{101})^2 + (\sigma_{d_0^{101}} d^{101}(\varphi))^2}. \quad \text{Eq. 8}$$

3.2. Full in-plane strain tensor quantification

The next stage of analysis required quantification of the strain tensors obtained through ring-core FIB milling and DIC ($-\Delta\varepsilon_\infty(\varphi)$) and the preliminary distributions of the (101) interplanar lattice strain ($\varepsilon^{101}(\varphi)$) obtained using literature values of d_0^{101} . The generic expression for in-plane residual strain variation ($\varepsilon(\varphi)$), can be identified from Mohr's circle strain construction as:

$$\varepsilon(\varphi) = \frac{\varepsilon_1 + \varepsilon_2}{2} + \frac{\varepsilon_1 - \varepsilon_2}{2} \cos 2(\varphi + \alpha), \quad \text{Eq. 9}$$

where ε_1 and ε_2 are the principal strains and α is the angular offset between the original and principal coordinate systems.

Least squares fitting of Equation 9 was performed on the strain distributions obtained through XRD and ring core milling using the inverse square of the standard deviation of each term as a weighting factor (Table 1). It is important to note that the use of the literature value of d_0^{101} has little or no effect on the magnitude of principal axis orientation angle α obtained from this fitting procedure (as demonstrated in Table 1), although it does affect the magnitude of the principal strains. It was found that the values obtained for the angular offset were 52.1° and 53.4° using the

ring-core and literature value of d_0^{101} XRD techniques respectively. This 1.2° difference is likely to have arisen from small misalignment during sample positioning in the two experiments. Therefore the approximation that the ring-core and XRD principal orientations were aligned was used for the rest of the analysis.

Table 1. Table showing fitted estimates and standard deviations of the principal strains, stresses and orientations for the ring-core and XRD stress/strain tensor analysis. The lattice parameters obtained from the literature and through least squares fitting (in both plane stress and plane strain) have been included for the XRD analysis.

Technique	d_0^{101} (Å)	ε_1^a (millistrain)	ε_2^a (millistrain)	σ_1^a (MPa)	σ_2^a (MPa)	α (degrees)
Ring-core	-	1.73 ± 0.007	1.26 ± 0.007	499 \pm 1.81	424 \pm 1.81	52.1 \pm 1.26
XRD Lit d_0^{101} ^b	2.9582 ± 0.0015	1.80 ± 0.007	1.44 ± 0.007	-	-	53.3 \pm 0.99
XRD Fitted d_0^{101} (Plane stress)	2.9586 ± 0.0004	1.67 ± 0.006	1.31 ± 0.007	489 \pm 1.72	432 \pm 1.65	53.2 \pm 0.97
XRD Fitted d_0^{101} (Plane strain)	2.9596 ± 0.0003	1.36 ± 0.006	0.96 ± 0.007	546 \pm 2.50	482 \pm 2.38	53.4 \pm 0.96

^a Compressive stress and strain values are positive.

^b Calculated using lattice parameters published by Shah et al. [55].

Careful consideration of the gauge volumes associated with the two techniques reveals that ring-core technique provides an estimate of the average strain in a $5 \mu\text{m}$ tall, $5 \mu\text{m}$ diameter near-interface cylinder, whereas the through sample penetration of the incident X-ray beam probes a $7.2 \times 9 \times 115 \mu\text{m}^3$ volume. Although these gauge volumes are both centred at the same location in the plane of the sample, the average out of plane conditions are different. In the case of the near-surface ring-core technique, the mechanical state can best be approximated as a state of plane stress. Therefore the principal stresses ($\widehat{\sigma}_1, \widehat{\sigma}_2$) and the associated standard deviations ($\sigma_{\widehat{\sigma}_1}, \sigma_{\widehat{\sigma}_2}$) can be determined using:

$$\widehat{\sigma}_1 = \frac{E}{1 - \nu^2} (\varepsilon_1 + \nu \varepsilon_2), \quad \text{Eq. 10}$$

$$\widehat{\sigma}_2 = \frac{E}{1 - \nu^2} (\varepsilon_2 + \nu \varepsilon_1), \quad \text{Eq. 11}$$

$$\sigma_{\hat{\sigma}_1} = \frac{E}{1 - \nu^2} \sqrt{(\sigma_{\varepsilon_1}^2 + \nu^2 \sigma_{\varepsilon_2}^2)}, \quad \text{Eq. 12}$$

$$\sigma_{\hat{\sigma}_2} = \frac{E}{1 - \nu^2} \sqrt{(\sigma_{\varepsilon_2}^2 + \nu^2 \sigma_{\varepsilon_1}^2)}, \quad \text{Eq. 13}$$

in which σ_{ε_1} and σ_{ε_2} are the standard deviations of the principal strains, E is Young's modulus of YPSZ and ν is Poisson's ratio of YPSZ. Estimates of E and ν were obtained from the literature and were given as 210 GPa [37] and 0.32 [56], respectively. No information was available on the likely distributions of these values and therefore they were treated as error-free measures. This approximation will artificially increase the precision of principal stress value determination (Table 1), but experimental errors are likely to dominate.

In the case of the XRD analysis the gauge volume can no longer be simply described as a simple planar mechanical state. In reality the XRD beam samples both the near surface regions (under near plane stress conditions) as well as bulk material (under generalised plane strain conditions). A review of the literature reveals that no agreement has yet been reached on the most representative plane state approximation in the case of transmission X-ray analysis [57, 58], although a the solutions of a few generalised cases have been published [59, 60]. The most suitable approximation is dependent upon the particular sample geometry (i.e. if the aspect ratio of the sample is large in the through beam direction then plain strain conditions are typically more suitable) and the average length scale of any structural/microstructural phenomena (i.e. in the case of a fibre composite system, the ratio between sample thickness and fibre diameter will dictate the most suitable approximation). For all practical purposes it can be noted however that the plane strain and plain stress assumptions can be considered as the upper and lower bound for the stress state within the region sampled by transmission XRD.

The YPSZ-porcelain prosthesis slice has a cross sectional area of approximately $10 \times 10 \text{ mm}^2$ and a thickness of $115 \text{ }\mu\text{m}$. The aspect ratio of the sample is therefore sufficiently large to approximate the system as a thin plate in a state of plane stress. On the other hand, in terms of

structural/microstructural features the only representative length scale is the nano-scale average grain size present in YPSZ. In this respect the sample thickness is far greater than the local feature length scales and the system may be better represented as a state of plane strain. In reality the XRD state sampled will be a weighted average of these two mechanical states and analysis was performed to determine the stress and strain response for both conditions.

3.3. The relationship between plane strain and plane stress

To compare the estimates of the residual stress state from XRD and FIB milling, the relationship between plane strain and plane stress conditions for the same sample needs to be determined. Therefore, in the analysis that follows, the connection between the plane strain state originally present in the YPSZ-porcelain system (which can be approximated as an infinite body) and the modified plane stress state induced during sample sectioning will be elucidated.

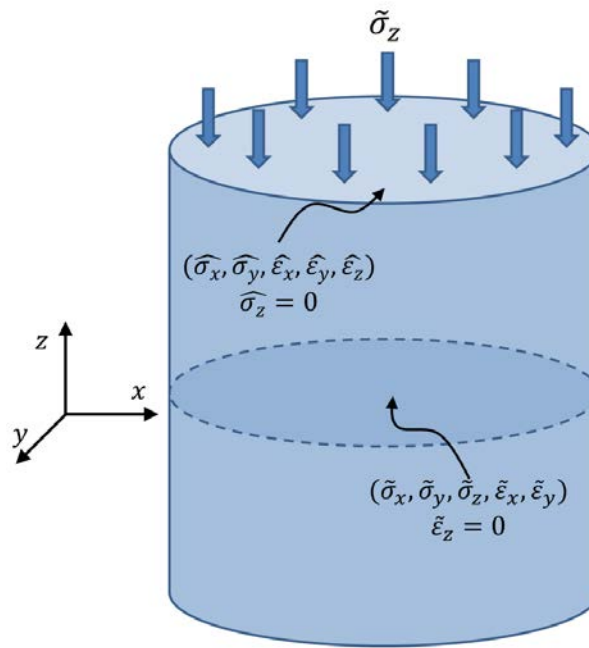


Figure 6. Schematic showing plane strain state present in YPSZ prosthesis prior to sectioning

$(\tilde{\sigma}_x, \tilde{\sigma}_y, \tilde{\sigma}_z, \tilde{\epsilon}_x, \tilde{\epsilon}_y, \tilde{\epsilon}_z = 0)$ and the plane stress conditions induced during sample sectioning $(\hat{\sigma}_x, \hat{\sigma}_y, \hat{\epsilon}_x, \hat{\epsilon}_y, \hat{\epsilon}_z, \hat{\sigma}_z = 0)$. The relationship between these two conditions can be determined by considering the influence of applying a uniform stress of magnitude $\tilde{\sigma}_z$ in a direction opposing the stress originally present.

A schematic of the plane strain and plane stress conditions is shown in Figure 6 in which the out of plane direction is parallel to the z axis and the principal stress orientations are aligned to the x, y coordinate system axes. In the unsectioned YPSZ body conditions of plane strain are present, the stresses in this system are given by $\tilde{\sigma}_x, \tilde{\sigma}_y$ and $\tilde{\sigma}_z$ and the in-plane strains by $\tilde{\epsilon}_x$ and $\tilde{\epsilon}_y$. Under the conditions of plane strain the out-of-plane strain component ($\tilde{\epsilon}_z$) must vanish at locations where the corresponding eigenstrain component is zero, i.e. must be set $\tilde{\epsilon}_z = 0$. If the out-of-plane eigenstrain component is present at the corresponding location, for example due to volumetric phase transformation, then it is necessary to set $\tilde{\epsilon}_z = -\epsilon_z^*$, where ϵ_z^* is the z direction eigenstrain component [61].

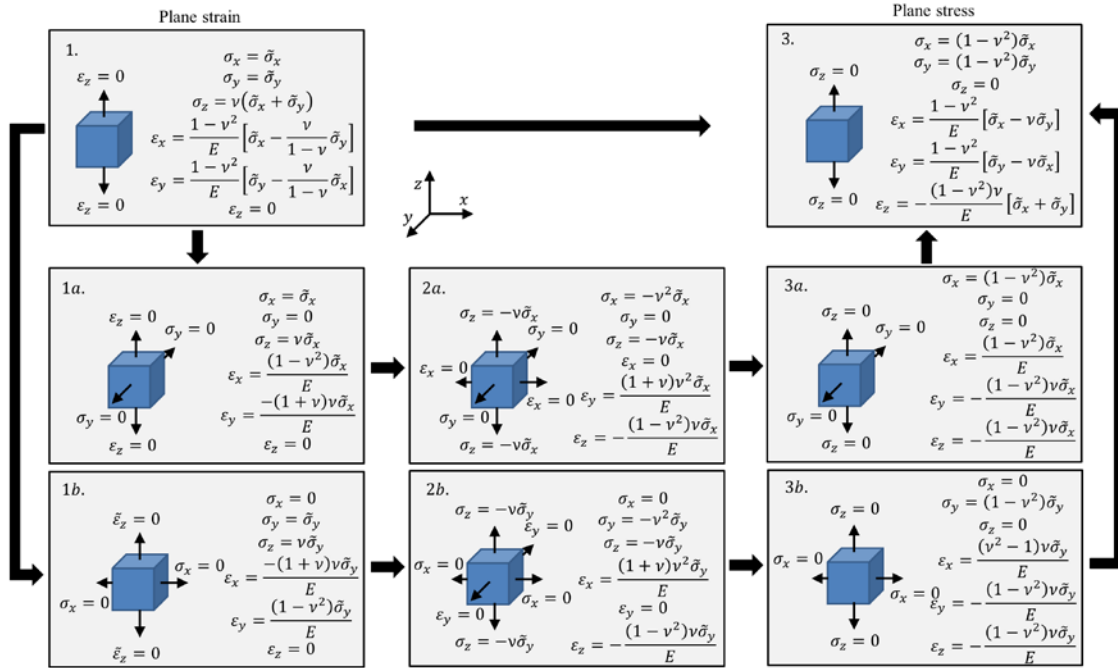


Figure 7. Schematic showing the relationship between original plane strain conditions and the condition approximating to a plane stress state. All relationships are written in terms of the in-plane stresses originally present ($\tilde{\sigma}_x$ and $\tilde{\sigma}_y$). The systematic decoupling of the x and y in plane strains, and the associated stress changes are shown in a and b.

Hooke's law can then be used to define the plane strain relationship between $\tilde{\sigma}_x, \tilde{\sigma}_y$ and $\tilde{\sigma}_z$:

$$\tilde{\epsilon}_z = 0 = \frac{1}{E} [\tilde{\sigma}_z - \nu(\tilde{\sigma}_x + \tilde{\sigma}_y)], \quad \text{Eq. 14}$$

$$\tilde{\sigma}_z = \nu(\tilde{\sigma}_x + \tilde{\sigma}_y). \quad \text{Eq. 15}$$

The full stress and strain state of the plane strain state can then be written solely in terms of $\tilde{\sigma}_x$ and $\tilde{\sigma}_y$ as shown in Figure 7, stress state 1.

In order to establish a relationship between the plane stress and plane strain states, the influence of the two in-plane residual stresses need to be uncoupled. By considering the two cases where $\tilde{\sigma}_y = 0$ and $\tilde{\sigma}_x = 0$ these two states can be determined as shown in Figure 7 (states 1a and 1b).

The application of stress equal and opposite to $\tilde{\sigma}_z$ can be used to simulate the introduction of a traction-free surface as shown in Figure 6. This will result in a surface stress value equal to zero in the z direction ($\sigma'_z = 0$), but will also modify the other stress and strain values. In the uncoupled stress states this is equivalent of applying stresses of $\sigma_z = -\nu\tilde{\sigma}_x$ and $\sigma_z = -\nu\tilde{\sigma}_y$ to the 1a and 1b states respectively.

Examination of stress state *a* reveals that the stress in the y direction is equal to zero and therefore that this orientation can be considered as having no displacement constraints in the y direction. Equivalently stress state *b* can be considered as having no constraints in the x direction. These two conditions can be used to decompose the stress change induced by the application of $-\tilde{\sigma}_z$ into two compatible tensor fields. In the case of state 2a the stress change in the y direction is zero and the strain change in the x direction is zero. Conversely, for state 2b the stress change in the x direction is zero and the strain change in the y direction is zero. The addition of stress states of these two types can be used to generate any arbitrary stress distribution.

In case 2a the stress state in the y and z directions are known. Using these values, the plane strain conditions in the x direction and Hooke's law, the stress in the x direction can be determined:

$$\varepsilon_x = 0 = \frac{1}{E}(\sigma_x - \nu\sigma_y - \nu\sigma_z) = \frac{1}{E}(\sigma_x - 0 + \nu^2\tilde{\sigma}_x), \quad \text{Eq. 16}$$

$$\sigma_x = -\nu^2 \tilde{\sigma}_x. \quad \text{Eq. 17}$$

Equivalent analysis can be performed for case $2b$ to determine that $\sigma_y = -\nu^2 \tilde{\sigma}_y$. Hooke's law can then be used to determine the strains in the other two principal directions as shown in Figure 7.

To determine the result of introducing the traction-free surface on the resultant stress and strain tensors, the decoupled intermediate states are added to give the plane stress states: $1a + 2a = 3a$ and $1b + 2b = 3b$. These two stress states are in conditions of plane stress in z direction but also in one of the other principal directions (the y direction for case a and the x direction for case b). Summation of states $3a$ and $3b$ provides expressions for the plane stress tensors in terms of the in-plane plain strain stresses ($\tilde{\sigma}_x$ and $\tilde{\sigma}_y$):

$$\widehat{\sigma}_x = (1 - \nu^2) \tilde{\sigma}_x, \quad \text{Eq. 18}$$

$$\widehat{\sigma}_y = (1 - \nu^2) \tilde{\sigma}_y, \quad \text{Eq. 19}$$

$$\widehat{\varepsilon}_x = \frac{1 - \nu^2}{E} [\tilde{\sigma}_x - \nu \tilde{\sigma}_y], \quad \text{Eq. 20}$$

$$\widehat{\varepsilon}_y = \frac{1 - \nu^2}{E} [\tilde{\sigma}_y - \nu \tilde{\sigma}_x], \quad \text{Eq. 21}$$

$$\widehat{\varepsilon}_z = -\frac{(1 - \nu^2)\nu}{E} [\tilde{\sigma}_x + \tilde{\sigma}_y]. \quad \text{Eq. 22}$$

These expressions reveal that the factor $(1 - \nu^2)$ relates the in-plane stresses under the conditions of plane strain to those modified by the introduction of the free surface.

3.3.1. Kolosov-Muskhelishvili plane eigenstrain potentials

In order to provide comparison with the analysis outlined above, the same plane eigenstrain problem of elasticity can be assessed using Kolosov-Muskhelishvili complex potentials; a well-established methodology which has previously been used to validate a wide range of mechanical interactions [62, 63]. The analysis starts with the fundamental solution for a point eigenstrain within an infinite plane solid, and goes onto exploit the integral expression for residual stress state that

arises due to an arbitrary distribution of eigenstrain within a bounded domain [64]. Comparisons between the plane strain and plane stress cases of the plane eigenstrain problem can then be drawn in order to determine the relationship between these two states.

In the Kolosov-Muskhelishvili complex potential formulation, all components of stress, displacement and strain are expressed in terms of two complex potential functions $\Phi(z)$, $\Omega(z)$ as follows [65]:

$$\sigma_{11} + \sigma_{22} = 2[\Phi(z) + \overline{\Phi(z)}], \quad \text{Eq. 23}$$

$$\sigma_{22} - i\sigma_{12} = [\Phi(z) + \overline{\Omega(z)} + (z - \bar{z})\overline{\Phi'(z)}], \quad \text{Eq. 24}$$

$$2\mu(u_{1,1} + iu_{2,1}) = [\kappa\Phi(z) - \overline{\Omega(z)} - (z - \bar{z})\overline{\Phi'(z)}], \quad \text{Eq. 25}$$

where $i = \sqrt{-1}$, $z = x_1 + ix_2 = x + iy$ as shown in Figure 8, $\Phi'(z) = d\Phi(z)/dz$, μ is the shear modulus and κ is the Kolosov constant which is equal to $3 - 4\nu$ for plane strain and $(3 - \nu)/(1 + \nu)$ for plane stress. The use of a comma followed by a subscript i indicates differentiation with respect to x_i , while a bar over a function denotes its complex conjugate.

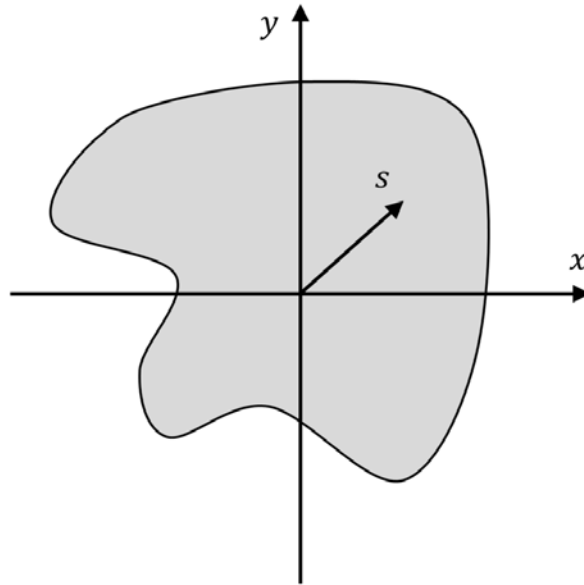


Figure 8. Schematic of eigenstrain domain A showing eigenstrain source point vector s .

The Kolosov-Muskhelishvili complex potentials for a point eigenstrain located at a source point $s = \xi + i\eta$ within an infinite plane solid (in which the position vector is given by $z = x + iy$) can be expressed in terms of two principal eigenstrain values and the principal direction $(\varepsilon_{x0}, \varepsilon_{y0}, \psi)$ as [66]:

$$\left\{ \begin{array}{l} \Phi_0(z) = \frac{\mu(\varepsilon_{y0} - \varepsilon_{x0})e^{2i\psi}}{\pi(1+\kappa)(z-s)^2}, \end{array} \right. \quad \text{Eq. 26}$$

$$\left\{ \begin{array}{l} \Omega_0(z) = \frac{\mu[2(\varepsilon_{y0} + \varepsilon_{x0}) - e^{2i\psi}(\varepsilon_{y0} - \varepsilon_{x0})]}{\pi(1+\kappa)(z-s)^2} + \frac{2\mu(\varepsilon_{y0} - \varepsilon_{x0})e^{2i\psi}}{\pi(1+\kappa)} \frac{(\bar{s} - s)}{(z-s)^3}. \end{array} \right. \quad \text{Eq. 27}$$

The expression in terms of principal eigenstrains and principal angle $(\varepsilon_{x0}, \varepsilon_{y0}, \psi)$ can be transformed to the form of expression in terms of eigenstrain components $(\varepsilon_{11}^*, \varepsilon_{22}^*, \varepsilon_{12}^*)$ referring to the global x - y coordinate system, leading to the alternative expressions:

$$\left\{ \begin{array}{l} \Phi_0(z) = \frac{\mu[(\varepsilon_{22}^* - \varepsilon_{11}^*) - 2i\varepsilon_{12}^*]}{\pi(1+\kappa)(z-s)^2} = \frac{\mu}{\pi(1+\kappa)} \phi(z, s), \end{array} \right. \quad \text{Eq. 28}$$

$$\left\{ \begin{array}{l} \Omega_0(z) = \frac{\mu\{2(\varepsilon_{11}^* + \varepsilon_{22}^*) - [(\varepsilon_{22}^* - \varepsilon_{11}^*) - 2i\varepsilon_{12}^*]\}}{\pi(1+\kappa)(z-s)^2} + \frac{2\mu[(\varepsilon_{22}^* - \varepsilon_{11}^*) - 2i\varepsilon_{12}^*]}{\pi(1+\kappa)} \frac{(\bar{s} - s)}{(z-s)^3} \\ \quad \quad \quad = \frac{\mu}{\pi(1+\kappa)} \omega(z, s) \end{array} \right. \quad \text{Eq. 29}$$

The Kolosov-Muskhelishvili complex potential due to the distribution of eigenstrain in the arbitrary domain A shown in Figure 8 can then be written as:

$$\left\{ \begin{array}{l} \Phi(z) = \frac{\mu}{\pi(1+\kappa)} \int_A \phi(z, s) dA = \frac{\mu}{\pi(1+\kappa)} \int_{\xi} \int_{\eta} \phi(z, \xi + i\eta) d\xi d\eta, \end{array} \right. \quad \text{Eq. 30}$$

$$\left\{ \begin{array}{l} \Omega(z) = \frac{\mu}{\pi(1+\kappa)} \int_A \omega(z, s) dA = \frac{\mu}{\pi(1+\kappa)} \int_{\xi} \int_{\eta} \omega(z, \xi + i\eta) d\xi d\eta, \end{array} \right. \quad \text{Eq. 31}$$

where Equations 28 and 29 now imply that $\varepsilon_{ij}^* = \varepsilon_{ij}^*(s)$ for $s \in A$.

The stress field outside the eigenstrain domain, $z \notin A$ is obtained by substituting Equations 30 and 31 into Equations 23-25 and can be written in a compact form as:

$$\sigma_{ij} = \frac{\mu}{\pi(1+\kappa)} f_{ij}(z). \quad \text{Eq. 32}$$

Here $f_{ij}(z)$ denotes the appropriate combination of functions $\Phi(z)$ and $\Omega(z)$. The common dimensional multiplier of these functions is given as $\mu/\pi(1 + \kappa)$.

The above expression needs to be modified for $z \in A$. The stress-strain relation in this case must be written to take into account strain additivity, i.e. the fact that total strain is written as the sum of elastic strain ε_{ml} and inelastic strain (eigenstrain) ε_{ml}^* as:

$$\varepsilon_{ml}^{\text{total}} = \varepsilon_{ml} + \varepsilon_{ml}^*. \quad \text{Eq. 33}$$

The stress-strain relationship is then written as:

$$\sigma_{ij} = c_{ijml}(\varepsilon_{ml}^{\text{total}} - \varepsilon_{ml}^*), \quad \text{Eq. 34}$$

leading to:

$$\sigma_{ij} = \frac{\mu}{\pi(1 + \kappa)} f_{ij}(z) - \frac{\mu}{\pi(1 + \kappa)} g_{ij}(z), \quad \text{Eq. 35}$$

where $g_{ij}(z)$ has the functional form of $f_{ij}(z)$, but with eigenstrain ε_{ml}^* playing the role of argument instead of the elastic strain ε_{ml} . Function $g_{ij}(z)$ assumes the value of zero outside the eigenstrain domain. Substituting the values of the Kolosov constant $\kappa = 3 - 4\nu$ for plane strain ($\tilde{\sigma}_{ij}$) and $\kappa = (3 - \nu)/(1 + \nu)$ for plane stress ($\widehat{\sigma}_{ij}$), the result obtained has the form:

$$\tilde{\sigma}_{ij} = \frac{\mu}{\pi(1 + 3 - 4\nu)} (f_{ij}(z) - g_{ij}(z)) = \frac{\mu}{4\pi(1 - \nu)} (f_{ij}(z) - g_{ij}(z)), \quad \text{Eq. 36}$$

$$\widehat{\sigma}_{ij} = \frac{\mu}{\pi[1 + (3 - \nu)/(1 + \nu)]} (f_{ij}(z) - g_{ij}(z)) = \frac{\mu(1 + \nu)}{4\pi} (f_{ij}(z) - g_{ij}(z)). \quad \text{Eq. 37}$$

Therefore, everywhere within a plane solid, both inside and outside the eigenstrain domain A , the relationship between plane stress and plane strain residual stress states that arise due to a particular plane eigenstrain distribution is given by:

$$\widehat{\sigma}_{ij}(x, y) = (1 - \nu^2) \tilde{\sigma}_{ij}(x, y). \quad \text{Eq. 38}$$

This expression has the same form as those developed in Equations 18 and 19.

3.3.2. Finite Element Analysis

FE simulation can be used as a fast and reliable tool for numerical validation of the analytical relationships between two stress states (for example, plane strain and plane stress) that arise in the body due to the presence of plane eigenstrain. Unconstrained 2D simulations of a rectangular region of YPSZ under plane stress and plane strain conditions were carried out for the case of a *plane eigenstrain* problem ($\varepsilon_z^* = 0$). The in-plane eigenstrains were given by an identical anisotropic 2D Gaussian distribution:

$$\varepsilon_x^*(x, y) = \varepsilon_y^*(x, y) = 1.25 \times 10^{-3} e^{-\left(\frac{x}{2}\right)^2} e^{-\left(\frac{y}{8}\right)^2}, \quad \text{Eq. 39}$$

where x and y are the coordinate positions. This localised peak of eigenstrain can be thought of as a basic constituent term in a wavelet transform or similar decomposition of an arbitrary eigenstrain field. In other words, if the transformation between plane strain and plane stress solutions is shown to be correct for this case, it is possible to assert with some justification that the result will also hold in the most generic cases that can be decomposed into superposition of such basic terms.

Following the introduction of eigenstrain, the consequence of post-processing (transformation) of the plane strain solution was then directly compared to the full plane stress FE results, as shown in Figure 9. The numerical discrepancy between the two approaches was found to be less than 0.5%, i.e. within the simulation error bounds. This provides numerical validation of the relations presented in Equations 19-22.

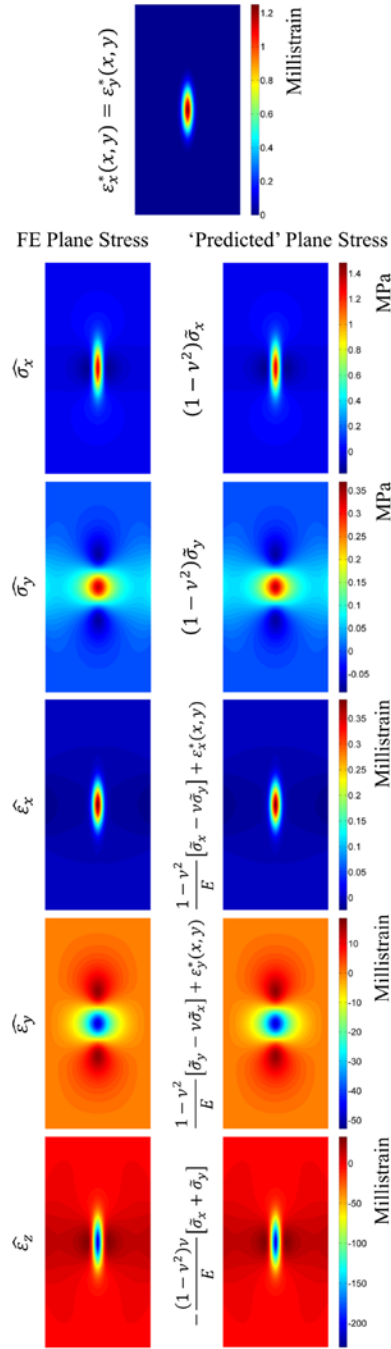


Figure 9. Result of 2D YPSZ FE simulations of residual stresses and strains induced by the application of 2D Gaussian eigenstrain distributions ($\epsilon_x^*(x,y)$ and $\epsilon_y^*(x,y)$). The results of the FE plane stress analysis are shown on the left of the figure and the comparable ‘predicted’ plane stress results obtained from the plane strain simulations are shown on the right. The expressions used to calculate these distributions are given next to each plot and are equal to the elastic responses given in equations 18-22 plus the eigenstrain contribution. The average difference between profiles is 0.5% which is associated with numerical errors in the simulation.

4. Results

Following the establishment of the relationship between the residual stress state according to plane stress or plane strain approximations (Equations 18 and 19), these expressions were used to estimate d_0^{101} for the plane strain approximation. Beginning with the plane stress elastic field solution, the in-plane residual stress determined by ring-core FIB milling were transformed into the corresponding estimates of plane strain. The interpretation of XRD strain measurements was then adjusted by varying the unstrained lattice parameter, and estimates of the corresponding stress components were calculated using plane strain relationships between strains and stresses:

$$\tilde{\sigma}_1 = \frac{E}{(1+\nu)(1-2\nu)} ((1-\nu)\varepsilon_1 + \nu\varepsilon_2), \quad \text{Eq. 40}$$

$$\tilde{\sigma}_2 = \frac{E}{(1+\nu)(1-2\nu)} ((1-\nu)\varepsilon_2 + \nu\varepsilon_1), \quad \text{Eq. 41}$$

$$\sigma_{\tilde{\sigma}_1} = \frac{E}{(1+\nu)(1-2\nu)} \sqrt{((1-\nu)^2\sigma_{\varepsilon_1}^2 + \nu^2\sigma_{\varepsilon_2}^2)}, \quad \text{Eq. 42}$$

$$\sigma_{\tilde{\sigma}_2} = \frac{E}{(1+\nu)(1-2\nu)} \sqrt{((1-\nu)^2\sigma_{\varepsilon_2}^2 + \nu^2\sigma_{\varepsilon_1}^2)}, \quad \text{Eq. 43}$$

where $(\sigma_{\tilde{\sigma}_1}, \sigma_{\tilde{\sigma}_2})$ are the standard deviations of the principal strains. The optimum value of the (101) lattice parameter was found to be 2.9596 Å, which corresponded to the principal stresses of 546 MPa and 482 MPa.

For the plane stress approximation, the refinement of d_0^{101} was performed by comparing the XRD principal strain values with the absolute values obtained through ring-core FIB milling (1.73×10^{-3} and 1.26×10^{-3}). The optimised magnitude of d_0^{101} was found to be 2.9586 Å, which corresponded to the principal strains of 1.67×10^{-3} and 1.31×10^{-3} . Equations 10-13 were then used to obtain the estimates of principal stresses and associated standard deviations included in Table 1.

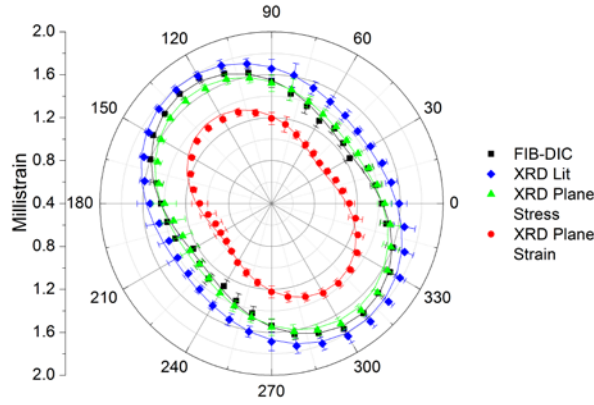


Figure 10. Polar plot of millistrain against angle φ showing strains obtained using the ring-core FIB-DIC technique and XRD using the literature, plane stress and plane strain refined values of d_0^{101} . The profiles obtained by least squares fitting of Equation 9 have been included for comparison. The error bars correspond to the 95% confidence intervals of each data point.

A polar plot of strain variation with angle φ is provided in Figure 10 showing the results obtained from the ring-core FIB milling and DIC approach along with the XRD results. The strain distributions obtained with the literature, plane strain and plane stress values of d_0^{101} have been included, along with the results of least squares fitting of Equation 9. The variation of residual stress with angle φ for the ring-core FIB milling and XRD approaches are shown in Figure 11.

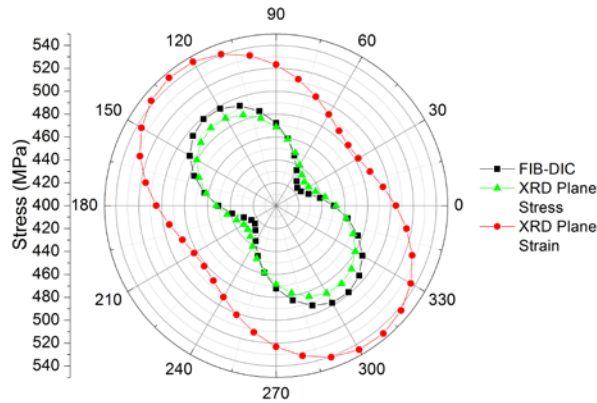


Figure 11. Polar plot of stress against angle φ showing the variations obtained using the ring-core FIB-DIC technique and XRD assuming plane stress and plane strain conditions.

5. Discussion

5.1. XRD analysis

A critical examination of the angular variation of strain obtained from XRD shown in Figure 10 reveals that it follows the required $\cos(2\varphi)$ functional form. This suggests that the lattice spacing captured during this analysis is representative of the full in-plane strain state present within the sample.

The sensitivity of strain calculation to the precise quantification of lattice spacing is also demonstrated in Figure 11. The use of the literature value of $d_0^{101} = 2.9582 \text{ \AA}$ produces a strain state which does not agree with the observations of the ring-core FIB milling and DIC approach. The refinement of this parameter assuming conditions of plane strain provides an upper bound value of $d_0^{101} = 2.9596 \text{ \AA}$, a change of 0.0014 \AA which is sufficient to decrease the principal strains by 0.45 millistrain on average. A lower bound for d_0^{101} can also be obtained by considering the situation where the XRD gauge volume is assumed to conform to plane stress conditions, leading to $d_0^{101} = 2.9586 \text{ \AA}$.

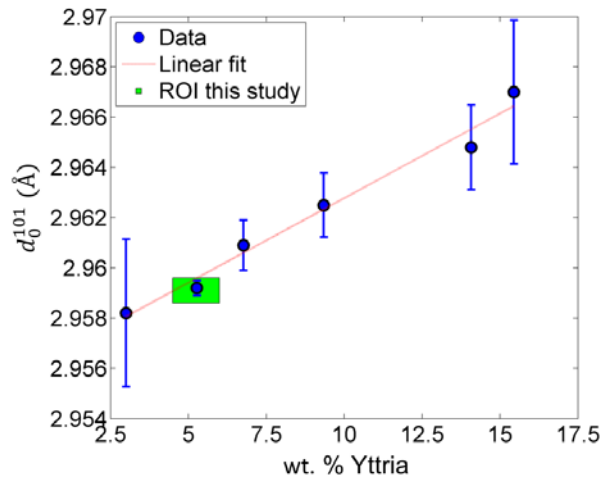


Figure 12. Plot of d_0^{101} against wt. % Yttria for the tabulated results in Table 2. The Region of Interest (ROI) associated with study has been bounded by the values of d_0^{101} calculated for the plane stress and plane strain conditions and the manufacturer's tolerances of the Yttria wt. % in Zenotec Zr Bridge [37]. A linear fit to the data has been included and the error bars indicate the 95% confidence intervals of the d_0^{101} values.

As previously discussed, the through thickness XRD gauge volume spans regions under the conditions of plane stress and plane strain. Therefore, the strain distribution determined through XRD interpretation corresponds to some sort of convolution between the two states, and plane strain and plane stress conditions serve as the upper and lower bounds respectively for the deformation state within the system.

Table 2. Table of YPSZ lattice parameters and the associated d_0^{101} lattice parameters for different wt. % of yttria (along with the associated standard deviations of each value). The reference, manufacturer and product name for each material has been included as well as the estimates obtained during this study.

Ref.	Manufacturer / Product Name	wt. % Yttria	a (Å)	c (Å)	d_0^{101} (Å)
[55]	Tosoh / TZ-3YE	3.0	3.605 ± 0.001	5.177 ± 0.002	2.9582 ± 0.0015
[67]	Z-Tech LLC / EF-Premium	5.3	3.6055 ± 0.0004	5.1797 ± 0.0002	2.9592 ± 0.0002
[37] ^a	Wieland Dental / Zenotec Zr Bridge	4.5 – 6.0	-	-	2.9586 ± 0.0004
[37] ^b			-	-	2.9599 ± 0.0003
[68]	Synthesised in house using: Merck / zirconium oxychloride Riedel-de Haën / yttrium oxide	6.8	3.6162 ± 0.0004	5.1576 ± 0.0006	2.6909 ± 0.0005
		9.3	3.6251 ± 0.0005	5.1401 ± 0.0008	2.9625 ± 0.0007
		14.1	3.6297 ± 0.0007	5.1394 ± 0.0010	2.9648 ± 0.0009
		15.4	3.6325 ± 0.0009	5.1426 ± 0.002	2.9670 ± 0.0015

^a This work – XRD plane stress approximation.

^b This work – XRD plane strain approximation.

A review of the literature was performed to assess the d_0^{101} estimates obtained. No quantitative information on the expected lattice parameters of Zenotech Zr Bridge [37] were identified however a range of YPSZ compositions were obtained and the results of the comparison are given in Table 2. Figure 12 provides a pictorial representation of the lattice spacing variation with wt. % of Yttria and reveals that this variation appears to correspond to the linear relationship. The Region Of Interest (ROI) associated with this study has also been included in this Figure 12. It is bounded by the plane strain and plane stress estimates of d_0^{101} and the manufacturer's tolerances for Yttria wt. % [37]. It can be seen that the lattice parameters published by Howard et al. [67] and the linear relationship

predicted by the literature values fall within this ROI. This suggests that the bounding values of d_0^{101} calculated using the plane stress and plane strain approximations in this study are likely to be reliable.

5.2. FIST ring-core FIB milling and DIC

Stress and strain tensor quantification using XRD is a well-established technique [21, 23] which can be used as a reference to assess and validate the quality of stress and strain evaluation using ring-core FIB milling and DIC. Comparisons of the angular strain variation shown in Figure 10 (and Table 1) reveal that the required $\cos 2\varphi$ relationship is also observed in the data sets obtained using ring-core FIB milling and DIC. The angular offset between the XRD and ring-core profiles is on average is a small value of 1.2° comparable to the sample mounting orientation error. This demonstrates that the two techniques are aligned with each other to a level of precision that is better than the scatter and experimental error that arises due to external factors.

The least squares fitting that has been performed between the plane stress XRD and ring-core analyses ensures that care must be taken when comparing the magnitudes of the principal strain values obtained. For example, if only one of the principal values were taken into consideration, optimisation of the interplanar spacing (d_0^{101}) could be used to exactly match the XRD and ring-core strain estimates in that direction. In contrast to this approach, optimisation of the interplanar spacing was instead performed simultaneously on both strain component values (x and y) using a single parameter (d_0^{101}). In this situation, the underlying lattice parameter variation is critical to the quality of fit observed. The optimised error between the two values was found to be ± 0.06 millistrain or approximately 4% of the strain value. This level of precision demonstrates that the principal strain relationships for the XRD and ring-core FIB milling techniques are very similar.

The excellent matching observed between the principal strain values also translates to the stress estimates determined in each case. In the case of plane stress the difference between the XRD and ring-core principal stress estimates were 10 MPa (2%) and -8 MPa (1.9%) for the 1 and 2 values respectively. Similar comparisons can be drawn with the plane strain results by dividing the stress

estimates by $(1 - \nu^2)$. In this case the offsets were 9 MPa (1.8%) and -9 MPa (2.1%) for the 1 and 2 values respectively.

A critical examination of the final stress state reveals that at $50 \mu\text{m}$ from the YPSZ-porcelain interface the YPSZ is in a highly compressed state (average plane stress value = 461 MPa , average plane strain value = 514 MPa) with a relatively small shear component (plane stress value $\tau_{max} = 37.5 \text{ MPa}$, plane strain value $\tau_{max} = 31 \text{ MPa}$). Although a number of mechanisms have been proposed to understand the generation of residual stress at this near-interface location [39, 69] only one nanoindentation study by Zhang et al. [41] has quantified the stress magnitude at a resolution comparable to this study. This analysis revealed that at $50 \mu\text{m}$ from the interface the average plane stress residual stress value in the YPSZ was between 475 and 511 MPa for porcelain coatings of comparable thickness to that applied in this study. The intrinsic variation between samples, and differing experimental techniques used to quantify the residual stress states in each case mean that some discrepancy is expected between these two sets of results. However, it can and should be noted that in general the plane stress ring-core FIB milling and DIC approach shows good agreement with XRD measurements and indentation.

6. Conclusions

The strain and stress tensors obtained using the FIST ring-core FIB milling and DIC method, and XRD show excellent agreement both in terms of angular orientation and principal strain and stress values. Realistic lattice spacing estimates obtained in this study and the agreement with residual stress values previously published in the literature demonstrates that the results obtained using the two techniques are highly consistent with each other and with current knowledge of the YPSZ-porcelain system.

This study has demonstrated the FIST FIB milling and DIC technique which is the first experimentally validated FIB based technique capable of quantifying the full in-plane tensor in a microscale gauge volume. The short experimental durations (~ 30 minutes), automated processing routines and well-defined confidence intervals associated with this technique ensure that this

approach offers a rapid, reliable and precise solution for experimental stress analysis at the micro-scale. This method overcomes the primary limitations of XRD strain tensor analysis: it provides an absolute measure of residual strain without the need for unstrained lattice parameter estimates, interrogates a well-defined 3D gauge volume, is suitable for use on amorphous materials, and can be readily implemented at a broad range of laboratory facilities.

This experimental technique has the potential to improve current understanding in the wide range of applications for which knowledge of the strain tensor is required within a microscale gauge volume. Although this method is a semi-destructive near-surface based technique, the approach can be extended to sub-surface measurements through appropriate sample sectioning. Although sectioning is known to modify the near-interface strain state, the analytical results presented here establish a link between the plane stress approximation of the near-surface residual stress state, and the plane strain approximation appropriate for material bulk. This result enables the evaluation of the original strain state present in the sample prior to sectioning or other material removal operations.

Alongside the validation of the FIST ring-core FIB milling and DIC technique that was the main focus of this experimental study, a simple technique has been presented that is capable of producing bounding estimates for the unstrained lattice spacing. This methodology is particularly well suited for the case where other lattice parameter determination methods have proved unsuccessful, for example due to limited quality diffraction patterns, or the impossibility of achieving the required spatial resolution in regions of high chemical gradients.

The derivation and numerical validation of the relationship between plane strain and plane stress conditions will also be useful in a broad range of mechanical studies, e.g. for continuously processed samples that contain sources of residual stress (eigenstrains) that are uniform along the axis of extrusion, and which are examined at their cross-sections.

7. Acknowledgements

The European Project EU FP7 project iStress (604646) is acknowledged for the funding support provided to the Multi-Beam Laboratory for Engineering Microscopy (MBLEM), where FIB milling experiments reported in this study were carried out. AMK also wishes to acknowledge the support of the Research Complex at Harwell for the Centre for In situ Processing Studies (CIPS).

References

1. Withers, P., *Residual stress and its role in failure*. Rep Prog Phys, 2007. **70**(12): p. 2211.
2. Tong, X., H. Zhang, and D.Y. Li, *Effect of Annealing Treatment on Mechanical Properties of Nanocrystalline α -iron: an Atomistic Study*. Scientific Reports, 2015. **5**: p. 8459.
3. Kreher, W. and A. Molinari, *Residual stresses in polycrystals as influenced by grain shape and texture*. Journal of the Mechanics and Physics of Solids, 1993. **41**(12): p. 1955-1977.
4. Sun, W. and H. Sehitoglu, *Residual stress fields during fatigue crack growth*. Fatigue & Fracture of Engineering Materials & Structures, 1992. **15**(2): p. 115-128.
5. Zheng, L.L., et al., *Intergranular strain evolution near fatigue crack tips in polycrystalline metals*. Journal of the Mechanics and Physics of Solids, 2011. **59**(11): p. 2307-2322.
6. Donegan, S.P. and A.D. Rollett, *Simulation of residual stress and elastic energy density in thermal barrier coatings using fast Fourier transforms*. Acta Materialia, 2015. **96**: p. 212-228.
7. Lee, C.-H. and K.-H. Chang, *Prediction of residual stresses in high strength carbon steel pipe weld considering solid-state phase transformation effects*. Computers & Structures, 2011. **89**(1-2): p. 256-265.
8. Srivastava, A., et al., *Micromechanics of plastic deformation and phase transformation in a three-phase TRIP-assisted advanced high strength steel: Experiments and modeling*. Journal of the Mechanics and Physics of Solids, 2015. **78**: p. 46-69.
9. Wang, L., G. Liu, and S. Bi. *Influence of shot peening on rolling fatigue life of case-hardened steel*. in *Advanced Mechatronic Systems (ICAMechS), 2012 International Conference on*. 2012. IEEE.
10. Gao, Y., *Improvement of fatigue property in 7050-T7451 aluminum alloy by laser peening and shot peening*. Materials Science and Engineering: A, 2011. **528**(10): p. 3823-3828.
11. Coules, H., et al., *High pressure rolling of low carbon steel weld seams: Part 2-Roller geometry and residual stress*. Science and Technology of Welding and Joining, 2013. **18**(1): p. 84-90.
12. Lunt, A.J.G., et al., *A State-of-the-art Review of Micron Scale Spatially Resolved Residual Stress Analysis by Ring-core Milling and Other Techniques*. J Strain Anal Eng, 2015. **50**(7): p. 426-444.
13. Rossini, N.S., et al., *Methods of measuring residual stresses in components*. Mater Design, 2012. **35**: p. 572-588.
14. Baimpas, N., et al., *Nano-scale mapping of lattice strain and orientation inside carbon core SiC fibres by synchrotron X-ray diffraction*. Carbon, 2014. **79**: p. 85-92.
15. Calahorra, Y., et al., *Young's Modulus, Residual Stress, and Crystal Orientation of Doubly Clamped Silicon Nanowire Beams*. Nano letters, 2015. **15**(5): p. 2945-2950.
16. Schorr, S., et al., *The complex material properties of chalcopyrite and kesterite thin-film solar cell absorbers tackled by synchrotron-based analytics*. Progress in Photovoltaics: Research and Applications, 2012. **20**(5): p. 557-567.
17. Kartal, M.E., F.P.E. Dunne, and A.J. Wilkinson, *Determination of the complete microscale residual stress tensor at a subsurface carbide particle in a single-crystal superalloy from free-surface EBSD*. Acta Materialia, 2012. **60**(13-14): p. 5300-5310.
18. Hosseinzadeh, F. and P. Bouchard, *Mapping multiple components of the residual stress tensor in a large P91 steel pipe girth weld using a single contour cut*. Experimental Mechanics, 2013. **53**(2): p. 171-181.
19. Traore, Y., et al., *Measurement of the residual stress tensor in a compact tension weld specimen*. Experimental Mechanics, 2013. **53**(4): p. 605-618.
20. Saito, Y. and S. Tanaka, *Residual Stress Tensor Distributions in Cracked Austenitic Stainless Steel Measured by Two-Dimensional X-Ray Diffraction Method*. Advanced Materials Research, 2014. **996**: p. 128-134.

21. Tamura, N., et al., *High spatial resolution grain orientation and strain mapping in thin films using polychromatic submicron x-ray diffraction*. Applied Physics Letters, 2002. **80**(20): p. 3724-3726.
22. Tamura, N., et al., *Scanning X-ray microdiffraction with submicrometer white beam for strain/stress and orientation mapping in thin films*. Journal of synchrotron radiation, 2003. **10**(2): p. 137-143.
23. Tamura, N., et al., *Submicron x-ray diffraction and its applications to problems in materials and environmental science*. Review of Scientific Instruments, 2002. **73**(3): p. 1369-1372.
24. Lachambre, J., et al., *Extraction of stress intensity factors for 3D small fatigue cracks using digital volume correlation and X-ray tomography*. International Journal of Fatigue, 2015. **71**: p. 3-10.
25. Marciszko, M., et al., *Stress Measurements in Polished Al-Mg Alloy and CrN Coating Using Multireflection Grazing Incidence Method*. Materials Science Forum, 2014. **783**: p. 2091-2096.
26. Lunt, A.J.G. and A.M. Korsunsky, *A Review of Micro-scale Focused Ion Beam Milling and Digital Image Correlation Analysis for Residual Stress Evaluation and Error Estimation*. Thin Solid Films, 2015. **In Press - Corrected Proof**.
27. Kang, K.J., et al., *A method for in situ measurement of the residual stress in thin films by using the focused ion beam*. Thin Solid Films, 2003. **443**(1-2): p. 71-77.
28. Krottenthaler, M., et al., *A simple method for residual stress measurements in thin films by means of focused ion beam milling and digital image correlation*. Surf Coat Tech, 2013. **215**(0): p. 247-252.
29. Sabate, N., et al., *Measurement of residual stress by slot milling with focused ion-beam equipment*. J Micromech Microeng, 2006. **16**(2): p. 254-259.
30. Korsunsky, A.M., M. Sebastiani, and E. Bemporad, *Residual stress evaluation at the micrometer scale: Analysis of thin coatings by FIB milling and digital image correlation*. Surf Coat Tech, 2010. **205**(7): p. 2393-2403.
31. Lunt, A.J.G. and A.M. Korsunsky, *Intragranular Residual Stress Evaluation Using the Semi-Destructive FIB-DIC Ring-Core Drilling Method*, 2014: Adv Mat Res. p. 8-13.
32. Song, X., et al., *Residual stress measurement in thin films at sub-micron scale using Focused Ion Beam milling and imaging*. Thin Solid Films, 2012. **520**(6): p. 2073-2076.
33. Song, X., et al., *Residual stress measurement in thin films using the semi-destructive ring-core drilling method using Focused Ion Beam*. Procedia Engineering, 2011. **10**(0): p. 2190-2195.
34. Sebastiani, M., et al., *Focused ion beam four-slot milling for Poisson's ratio and residual stress evaluation at the micron scale*. Surf Coat Tech, 2014. **251**: p. 151-161.
35. Sebastiani, M., et al., *Depth-resolved residual stress analysis of thin coatings by a new FIB-DIC method*. Mater Sci Eng: A, 2011. **528**(27): p. 7901-7908.
36. Bemporad, E., et al., *A critical comparison between XRD and FIB residual stress measurement techniques in thin films*. Thin Solid Films, 2014. **572**(0): p. 224-231.
37. Zenotec Zr Bridge. 10/09/15 Available from: <http://www.wieland-dental.de/en/products/zenotec/materials/zenotec-zr-bridge/>.
38. IPS e.max Ceram. 19/02/15 Available from: <http://www.ivoclarvivadent.co.uk/en/products/all-ceramics/ips-emax-technicians/ips-emax-ceram>.
39. Mainjot, A.K., et al., *Influence of zirconia framework thickness on residual stress profile in veneering ceramic: Measurement by hole-drilling*. Dental Materials, 2012. **28**(4): p. 378-384.
40. Baldassarri, M., et al., *Residual stresses in porcelain-veneered zirconia prostheses*. Dental Materials, 2012. **28**(8): p. 873-879.

41. Zhang, Y., M. Allahkarami, and J. Hanan, *Measuring residual stress in ceramic zirconia–porcelain dental crowns by nanoindentation*. J Mech Behav Biomed Mater, 2012. **6**: p. 120-127.
42. Korsunsky, A.M., et al., *Strain tomography of polycrystalline zirconia dental prostheses by synchrotron X-ray diffraction*. Acta Materialia, 2011. **59**(6): p. 2501-2513.
43. Silva, N.R.F.A., et al., *Reliability of Metalloceramic and Zirconia-based Ceramic Crowns*. Journal of dental research, 2010. **89**(10): p. 1051-1056.
44. Costa, A.K.F., et al., *The strength of sintered and adhesively bonded zirconia/veneer-ceramic bilayers*. Journal of Dentistry, 2014. **42**(10): p. 1269-1276.
45. Roberts, O., et al., *A Study of Phase Transformation at the Surface of a Zirconia Ceramic*. Proc WCE, 2014. **2**.
46. Lunt, A.J.G., et al., *Calculations of single crystal elastic constants for yttria partially stabilised zirconia from powder diffraction data*. J Appl Phys, 2014. **116**(5): p. 053509.
47. Mochales, C., et al., *Monoclinic phase transformations of zirconia-based dental prostheses, induced by clinically practised surface manipulations*. Acta Biomaterialia, 2011. **7**(7): p. 2994-3002.
48. Lunt, A.J.G., et al., *A Comparative Transmission Electron Microscopy, Energy Dispersive X-ray Spectroscopy and Spatially Resolved Micropillar Compression Study of the Yttria Partially Stabilised Zirconia–Porcelain Interface in Dental Prosthesis*. Thin Solid Films, 2015. **In Press - Corrected Proof**.
49. Lunt, A.J.G., et al., *Tensile Secondary Creep Rate Analysis of a Dental Veneering Porcelain*. Thin Solid Films, 2015. **In Press - Corrected Proof**.
50. Lunt, A.J.G., T.K. Neo, and A.M. Korsunsky, *An Electron Microscopy Study of Sintering in Three Dental Porcelains*. Proc WCE, 2015. **2**.
51. Korsunsky, A.M., et al., *Multi-Beam Engineering Microscopy-a Versatile Tool for Optimal Materials Design*. Proc IMCECS, 2015. **2**.
52. Eberl, C., et al., *Digital image correlation and tracking*. MatLabCentral, Mathworks file exchange server, 2006. **FileID - 12413**.
53. Salvati, E., et al., *An Investigation of Residual Stress Gradient Effects in FIB-DIC Micro-Ring-Core Analysis*. Proc IMCECS, 2015. **2**.
54. Salvati, E., et al., *On the Accuracy of Residual Stress Evaluation from Focused Ion Beam DIC (FIB-DIC) Ring-core Milling Experiments*. Proc ICNFA'15 2014. **265**.
55. Shah, K., J. Holloway, and I. Denry, *Effect of coloring with various metal oxides on the microstructure, color, and flexural strength of 3Y-TZP*. Journal of Biomedical Materials Research Part B: Applied Biomaterials, 2008. **87**(2): p. 329-337.
56. Della Bona, A., et al., *Characterization and surface treatment effects on topography of a glass-infiltrated alumina/zirconia-reinforced ceramic*. Dental Materials, 2007. **23**(6): p. 769-775.
57. Korsunsky, A.M., et al., *Fast residual stress mapping using energy-dispersive synchrotron X-ray diffraction on station 16.3 at the SRS*. Journal of synchrotron radiation, 2002. **9**(2): p. 77-81.
58. Withers, P.J., et al., *Recent advances in residual stress measurement*. International Journal of Pressure Vessels and Piping, 2008. **85**(3): p. 118-127.
59. Ballard, P. and A. Constantinescu, *On the inversion of subsurface residual stresses from surface stress measurements*. Journal of the Mechanics and Physics of Solids, 1994. **42**(11): p. 1767-1787.
60. Moore, M. and W. Evans, *Mathematical correction for stress in removed layers in X-ray diffraction residual stress analysis*, 1958, SAE Technical Paper.
61. Korsunsky, A., *Eigenstrain analysis of residual strains and stresses*. The Journal of Strain Analysis for Engineering Design, 2009. **44**(1): p. 29-43.
62. McPhedran, R.C. and A.B. Movchan, *The Rayleigh multipole method for linear elasticity*. Journal of the Mechanics and Physics of Solids, 1994. **42**(5): p. 711-727.

63. Hill, R., *On steady plane flows in classical elasticity*. Journal of the Mechanics and Physics of Solids, 1985. **33**(3): p. 315-322.
64. Korsunsky, A.M., *Fundamental eigenstrain solutions for axisymmetric crack problems*. Journal of the Mechanics and Physics of Solids, 1995. **43**(8): p. 1221-1241.
65. Muskhelishvili, N.I., *Some basic problems of the mathematical theory of elasticity* 2013: Springer Science & Business Media.
66. Ma, L., *Fundamental formulation for transformation toughening*. International Journal of Solids and Structures, 2010. **47**(22): p. 3214-3220.
67. Howard, C., R. Hill, and B. Reichert, *Structures of ZrO₂ polymorphs at room temperature by high-resolution neutron powder diffraction*. Acta Crystallographica Section B: Structural Science, 1988. **44**(2): p. 116-120.
68. Lamas, D.G. and N.E. Walsöe De Reca, *X-ray diffraction study of compositionally homogeneous, nanocrystalline yttria-doped zirconia powders*. Journal of Materials Science, 2000. **35**(22): p. 5563-5567.
69. Swain, M.V., *Unstable cracking (chipping) of veneering porcelain on all-ceramic dental crowns and fixed partial dentures*. Acta Biomaterialia, 2009. **5**(5): p. 1668-1677.

Vitae



Alexander J. G. Lunt is a stipendiary lecturer and DPhil student at Christ Church, Oxford, UK. He completed his MEng at the University of Oxford in 2012 where he was awarded the Institute of Mechanical Engineers Best Student Award. His primary research interest is the characterisation of the micromechanical behaviour of metals and ceramics using non-destructive techniques, microscopy and micro-scale mechanical testing. He has co-authored over 20 international journal articles including work in *Carbon*, *Acta Biomaterialia* and *Journal of Applied Physics*.



Enrico Salvati is a second-year DPhil candidate funded by EU FP7 collaborative research project iSTRESS. Enrico is also a Trinity College member and Visiting Staff member at the Research Complex at Harwell (UK). His research interest concerns the development of FIB-DIC micro ring core for the evaluation of residual stress, quantification of residual stress ahead crack tip using hi-resolution Synchrotron Powder Diffraction and FIB-FIC, Fatigue in metallic material and Finite Element Modelling.



Lifeng Ma is a professor at the Department of Engineering Mechanics, Xi'an Jiaotong University, China. His research interest is focused towards the theoretical aspects of applied mechanics including elasticity, plasticity, fracture, contact, inclusion mechanics, finite deformation, and the mechanics of liquid-solid interfaces.



Igor P. Dolbnya is a Scientist at Diamond Light Source, UK. His main research interests and expertise are in X-ray microscopy, small- and wide-angle X-ray scattering and diffraction as applied to different areas in materials science and soft condensed matter: e.g. physics, processing and microstructure properties of polymers, phase transitions phenomena in soft matter, studies of structure and dynamics of liquid crystals, colloids and colloidal crystals. He also has a prominent experience and record in developing the synchrotron radiation instrumentation and technology such as Synchrotron Beamlines, X-ray optics and detectors.



Dr Neo Tee Khin is a Dental Specialist in Prosthodontics with Specialist Dental Group[®], Singapore. He is also an Adjunct Senior Lecturer with the National University of Singapore and a Consultant at the National University Hospital. He is a Diplomate of the American Board of Prosthodontics. Dr Neo has a special interest in dental implants, crowns and aesthetic dentistry.



Alexander M. Korsunsky is a world-leader in engineering microscopy of materials and structures for optimisation of design, durability and performance. He heads the Multi-Beam Laboratory for Engineering Microscopy (MBLEM) at Oxford, and Centre for In situ Processing Science (CIPS) at the Research Complex at Harwell. He consults Rolls-Royce on residual stress and structural integrity, and is Editor-in-Chief of *Materials & Design*, an interdisciplinary international Elsevier journal (2014 IF=3.5). Korsunsky's research interests concern developing new materials and means of their fabrication and characterisation, and improving the integrity and reliability of engineered and natural structures, from high-performance metallic alloys to polycrystalline ceramics.

Contributions

Alexander J. G. Lunt – Main researcher, developed code to implement FIST FIB-DIC, implemented FIB milling and performed ring-core analysis. Prepared samples and ran XRD experiment.

Enrico Salvati – Implemented FE simulations necessary to numerically validate analytical and theoretical proofs.

Lifeng Ma – Derived the Kolosov-Muskhelishvili plane eigenstrain potential proof of the relationship between plane stress and plane strain.

Igor P. Dolbina – Beamline scientist during XRD experiment, helped optimise setup to ensure successful micro-focus arrangement.

Tee K. Neo – Provided samples, insight and initial motivation for studying the YPSZ-porcelain interface residual stress state in dental prostheses.

Alexander M. Korsunsky – Senior researcher for this study. Provided the initial idea behind FIST ring-core milling, led the XRD experiment and helped complete the Kolosov-Muskhelishvili plane eigenstrain potential proof.